Adaptive Optics for Astronomy

Ronald R. Parenti

During the last decade optical astronomy has played an increasingly important role in our understanding of the universe, and many recent discoveries can be directly attributed to revolutionary improvements in telescope design. At least 10 optical systems with apertures exceeding 3.5 m are currently available to the scientific community, and several telescopes in the 8-to-10-m class are now under construction. Although the light-gathering properties of these new telescopes are remarkable, at visible wavelengths their resolution is ultimately limited by phase distortions associated with atmospheric turbulence. Even under excellent seeing conditions, the imaging quality of these systems in the visible is seldom better than that obtainable from a 20-cm receiver.

Recent changes in military security guidelines have now made it possible to apply technology developed for high-energy laser-beam control to the problem of turbulence compensation for astronomy. In particular, the combination of high-bandwidth adaptive optics and synthetic-beacon sources offers the potential for near-diffraction-limited resolution at all optical wavelengths. This article investigates the principal design issues associated with the construction of adaptive optics systems for dim-target imaging, and develops quantitative performance estimates for a 4-m telescope.

The effects of atmospheric turbulence have hindered astronomers since the invention of the telescope, and the current trend toward ever larger collection apertures has made the search for a solution to this problem even more important [1, 2]. This limitation was one of the principal motivations for the Hubble project [3]. Other proposals to enhance seeing include placing observatories on the moon [4]. The recent Bahcall Committee report, which establishes research priorities in astronomy for the next decade, recognized this problem and included a strong recommendation for funding specifically earmarked for the development of methods to improve the resolution of terrestrial observatories [5].

Figure 1 shows a simplified description of the physical processes that produce image distortion. For vacuum propagation, light from a distant point source would reach a collection aperture with uniform amplitude and phase. The far-field diffraction pattern produced by a perfect circular aperture is the familiar Airy disk, which has an angular extent in output space approximately equal to the radiation wavelength λ divided by the aperture diameter D. For a 4-m telescope operating in the visible, λ / D corresponds to 0.03 arc sec.

When light passes through the earth's atmosphere, the phase of each collected ray depends on the product of the path length and the refractive index of the medium. Thermal fluctuations as small as a tenth of a degree can produce optical-path variations corresponding to several wavelengths across the diameter of the receiver. A statistical description of the perturbed wavefront derives from the works of A. Kolmogorov [6] and V.I. Tatarski [7]; in subsequent work it was shown that the long-exposure image produced by a large telescope subtends a *seeing angle* of λ / r_0, where r_0 is the turbulence coherence length [8]. Under good seeing conditions the seeing angle can be as small as 0.4 arc sec. For a 4-m telescope this angle represents a degradation of more than an order of magnitude in spatial resolution and over a factor of 100 reduction in image intensity. Although speckle interferometry has been applied with some success to mitigate the effects of atmospheric turbulence, this technique is

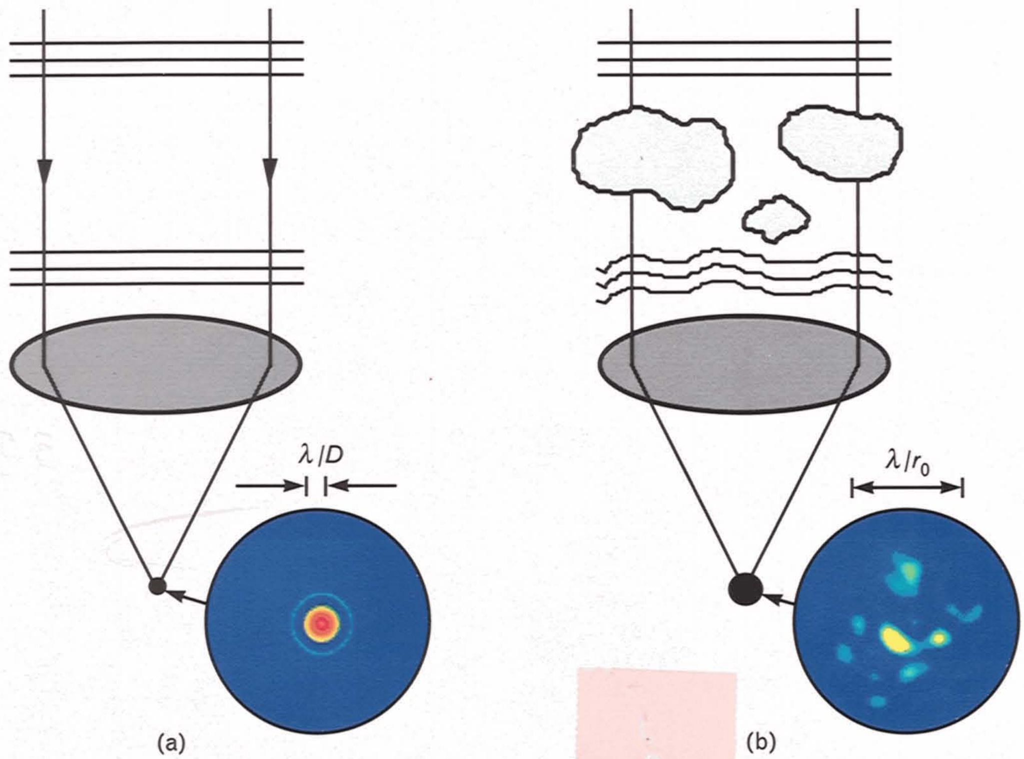

FIGURE 1. Comparison of imaging resolution of (a) a diffraction-limited receiver and (b) a telescope viewing through atmospheric turbulence. The far-field diffraction pattern produced by a perfect circular aperture is the familiar Airy disk, which has an angular extent in output space approximately equal to the radiation wavelength λ divided by the aperture diameter D. The point-spread function for turbulence can be characterized as a random distribution of diffraction-limited speckles covering an angular region of diameter λ/r_0.

useful only for recovering the images of relatively bright objects (see the box entitled "Speckle Interferometry").

Adaptive optics refers to a set of techniques that corrects turbulence-induced phase distortions by mechanically deforming a reflective surface in the optical train of the telescope. The compensation element, known as a *deformable mirror*, is the active component in a complex servo system that also includes a wavefront sensor to detect residual phase errors. Figure 2 illustrates a diagram of a modern system that closely resembles the conceptual design first proposed by H.W. Babcock in the early 1950s [9].

In the mid-1970s Lincoln Laboratory became one of the first research organizations to investigate the utility of adaptive optics for laser-beam-control applications. The first small-scale adaptive optics systems were constructed during that period. An excellent review of that early work was compiled by J.W. Hardy [10], and a more current treatment of the subject is found in the article by Darryl P. Greenwood and Charles A. Primmerman in this issue [11].

Because of the cost of developing high-performance adaptive optics hardware, virtually all of this research has been funded by the Department of Defense, whose primary mission has been the construction of laser weapon systems. It was quickly recognized that a fundamental problem exists in engagements involving *uncooperative targets*, which are satellites that do not carry a bright beacon that can be viewed by the wavefront sensor. Figure 3 shows a typical engagement scenario in which a satel-

SPECKLE INTERFEROMETRY

MODERN ASTRONOMY has not been without resources in dealing with the effects of turbulence. In 1970 A. Labeyrie observed that short-exposure celestial images are highly structured and are composed of an array of discrete spots, or *speckles* [1]. Each speckle corresponds to a diffraction-limited replica of the object under observation, and these images can be integrated by using Fourier transform techniques.

Unfortunately, speckle interferometry suffers from a number of serious limitations. The approach originally proposed by Labeyrie yields the object's autocorrelation function rather than a true image, because of phase information lost in the construction of the specklegram. For simple objects such as binary stars, all of the important data are readily recovered (see Figure A), but for complex bodies the reconstruction problem is more difficult. Recently a number of innovative processing methods have been proposed to recover both the phase and intensity data in the Fourier domain of the image [2–5].

A more serious concern relates to the signal-to-noise requirements of these computational techniques. J.W. Beletic [6] has shown that the effective efficiency of the process of converting input photons into an object reconstruction is inversely proportional to the product of the number of speckles in each image and the square root of the number of image samples. For nominal seeing conditions (approximately one arc second) and exposure times (approximately one hour), this collection efficiency can be as small as 10^{-5}. As a result, high-quality images are obtainable only from relatively bright sources.

References

1. A. Labeyrie, "Attainment of Diffraction Limited Resolution in Large Telescopes by Fourier Analyzing Speckle Patterns of Star Images," *Astron. Astrophys.* **6**, 85 (1970).
2. K.T. Knox and B.J. Thompson, "Recovery of Images from Atmospherically Degraded Short-Exposure Photographs," *Astrophys. J.* **193**, L-45 (1974).
3. C.R. Lynds, S.P. Worden, and J.W. Harvey, "Digital Reconstruction Applied to Alpha Orionis," *Astrophys. J.* **207**, 174 (1976).
4. R.H. Bates and F.M. Cady, "Towards True Imaging by Wideband Speckle Interferometry," *Opt. Commun.* **3**, 365 (1980).
5. W.I. Beavers, D.E. Dudgeon, J.W. Beletic, and M.T. Lane, "Speckle Imaging through the Atmosphere," *Lincoln Laboratory J.* **2**, 207 (1989).
6. J.W. Beletic, "Speckle Imaging of Complicated Objects," Ph.D. Thesis, Harvard University, Cambridge, MA, 1989.

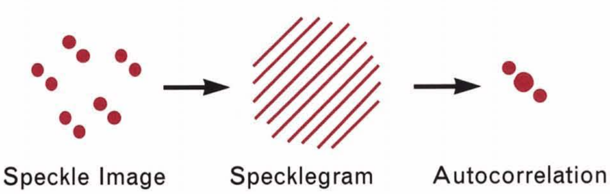

FIGURE A. Each speckle of a short-exposure binary-star image is comprised of a pair of spots having the same separation and orientation. If the star is dim these quantities often cannot be extracted from a single exposure. Integrating the power spectra of many such images forms a specklegram from which the object's autocorrelation function can be derived through an inverse transformation.

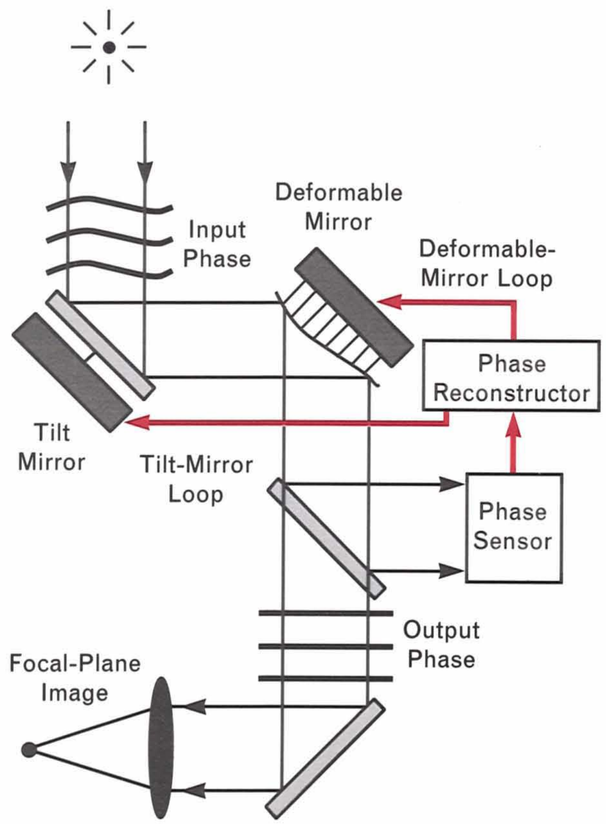

FIGURE 2. Essential components of an adaptive optics phase-compensation system. The first derivative of the phase difference between the incoming wavefront and the surface figure imposed by the tilt and deformable mirrors is measured by the phase sensor. The residual phase error is computed by the phase reconstructor and subsequently applied to the two active optical elements.

lite in low-earth orbit is moving at a velocity *v*. To intercept this target, a laser beam projected from a ground-based station must point ahead of the object by an angle of $2v/c$, where c is the speed of light. For low-earth-orbit satellites the point-ahead angle is approximately 50 μrad (10 arc sec), which is much larger than the *isoplanatic angle* within which phase distortions are highly correlated. Thus a measurement of the wavefront along the tracking path would be useless in correcting turbulence along the propagation path.

Although imaging celestial bodies does not require a point-ahead geometry, most objects of interest to astronomers provide too little light to make an accurate wavefront measurement. Thus astronomers encounter a similar problem in wavefront correction—the lack of a suitable reference source, or *beacon*, along the propagation path.

The first viable solution to this problem was proposed by J. Feinleib in 1982 [12] and later independently discovered by R. Foy and A. Labeyrie in 1985 [13]. The basic concept is simple and uses backscattered light from a powerful laser that is focused at a point in the atmosphere near the top of the turbulence region. This backscattered radiation from molecules and particulates is viewed by the wavefront sensor, which is temporally gated to restrict the illumination volume to which it is sensitive. Known as a *synthetic beacon*, or *laser guide star*, this source can be placed in any direction in the sky and made intense enough to permit accurate phase measurements.

The quality of the phase measurement afforded by an artificial source is limited by the dissimilarity in range between the beacon and the object, which leads to an error known as *focal anisoplanatism*. This effect decreases as beacon altitude increases, although at altitudes above 15 or 20 km the Rayleigh return from a laser of reasonable power becomes too small to be useful. To overcome this problem we can use multiple sources at low altitude [14] or exploit resonance backscatter from a stable layer of sodium atoms that resides in the mesosphere at an altitude of 90 km [15].

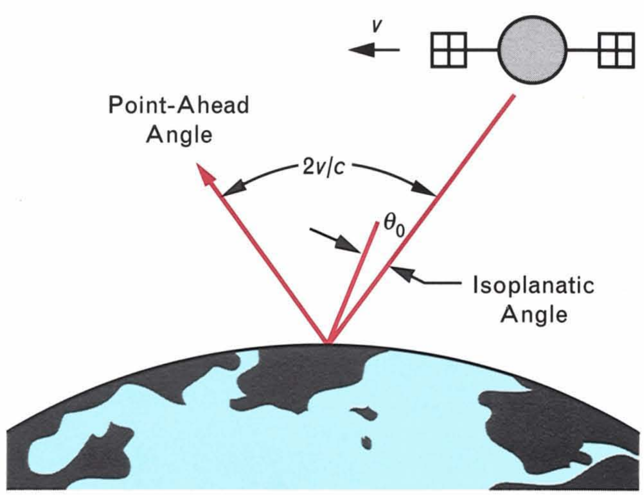

FIGURE 3. Engagement geometry for propagating a laser beam to a satellite. To intercept the target the laser must be pointed ahead of the tracking direction by an angle of $2v/c$. At visible wavelengths the point-ahead angle is much larger than the turbulence isoplanatic angle θ_0.

Although the synthetic-beacon concept is easy to describe, its reduction to practice involved one of the most complex systems ever constructed by Lincoln Laboratory. In an experimental program referred to as Short-Wavelength Adaptive Techniques (SWAT), a system incorporating a 241-actuator deformable mirror was mated to a 60-cm telescope operated at the top of Mount Haleakala in Maui, Hawaii [16]. A set of dye lasers were used to project synthetic Rayleigh beacons to altitudes as high as 7 km [17]. Over the past two years, both Lincoln Laboratory and the Phillips Laboratory have successfully demonstrated compensated imaging with guide-star systems. In 1991 the classification restrictions that had kept this work secret were modified and both the underlying theory and the experimental results were released to the open literature [14, 15, 18, 19].

The purpose of this article is to provide some insight into the main issues that affect the design of adaptive optics systems for large-aperture telescopes. Although the relationships developed have general application for high-performance beam control, this analysis is specifically directed toward the astronomy community, which may be constrained to compromise performance in exchange for substantial reductions in system cost and complexity. To identify the optimal design point in this multidimensional decision space we must develop a set of standards against which each of the principal hardware components can be evaluated. The end result of this process is a set of baseline constructs that balance complexity, performance, and overall utility.

Real-Time Adaptive Optics for Imaging Applications

An adaptive optics system can be thought of as a highly parallel servo device that simultaneously nulls the phase fluctuations of the incoming wavefront at many discrete locations over a two-dimensional field. Figure 2 illustrates how this mechanical correction is performed in the pupil plane of the telescope. The root-mean-square (rms) difference between the optical phase imposed by the deformable mirror and the incident distortion is a convenient measure of the quality of the average phase correction.

For systems using a cooperative beacon, the principal sources of error derive from the finite spatial resolution of the control surface and finite servo bandwidth. If the beacon is a faint object such as a dim star, then measurement errors introduced by the wavefront sensor will also affect performance. To quantify these effects we must first briefly review the more important statistical properties of atmospheric turbulence.

Spatial and Temporal Characteristics of Turbulence

According to theory developed by Kolmogorov [6], temperature fluctuations that give rise to optical turbulence originate as large-scale eddies that transmit energy without loss to progressively smaller disturbances. The refractive-index structure function $D_n(r)$ is found to be isotropic and proportional to the 2/3 power of the scalar distance r,

$$D_n(r) = C_n^2(h)\, r^{2/3} ,$$

where $C_n^2(h)$ represents the average turbulence strength as a function of altitude h. Calculations of turbulence effects typically involve integrals of the $C_n^2(h)$ profile that have the form

$$\mu_n = \int C_n^2(h)\, h^n \, dh ,$$

where μ_n is known as the nth turbulence moment.

The coherence length r_0 is the most important descriptor of the overall strength of turbulence-induced perturbations [8]:

$$r_0 = \left\{0.423\, k_c^2 \sec(\zeta)\, \mu_0\right\}^{-3/5} .$$

Here ζ is the zenith angle of the viewing path and $k_c = 2\pi/\lambda_c$ is the wave number of the radiation imaged onto a camera at the focus of the telescope. An aperture of dimension r_0 produces a near-diffraction-limited image that appears to change position as the atmosphere evolves with time. This parameter establishes the spatial dimensions of a *subaperture* within which a unique phase error can be measured and subsequently corrected by the movement of a single degree of freedom on the deformable mirror.

The temporal characteristics of turbulence are often modeled on the assumption that turbulence can be described as a set of frozen layers that move across the aperture at speeds that vary as a function of altitude. For simplicity, the direction of motion is usually assumed to be perpendicular to the plane containing the zenith angle. The velocity moments have the form

$$v_n = \int C_n^2(h)\, v^n(h)\, dh\,,$$

where $v(h)$ is the wind-velocity profile. A *critical time constant* τ_0, which derives from Greenwood [20], specifies the interval over which turbulence remains essentially unchanged:

$$\tau_0 = \left\{2.91\, k_c^2 \sec(\zeta)\, v_{5/3}\right\}^{-3/5}.$$

This frozen-turbulence model predicts a power spectrum that has an 8/3-power dependence over most of the range of interest.

Another quantity of interest is the usable field of view of a compensated-imaging system. This parameter is related to the isoplanatic angle θ_0, where

$$\theta_0 = \left\{2.91\, k_c^2 \sec^{8/3}(\zeta)\, \mu_{5/3}\right\}^{-3/5}. \qquad (1)$$

Objects within an angular radius θ_0 from the beacon direction can be imaged with good fidelity. Figure 4 provides a graphic description of the physical processes that govern r_0, τ_0, and θ_0.

To attach numerical values to these turbulence parameters, we must establish baseline profiles for turbulence and wind velocity. During the last two decades several dozen models have been developed in an attempt to describe profile measurements made at various locations throughout the world. For daytime conditions at inland sites, the SLC-Day turbulence model (which was standardized under the Submarine Laser Communications program) and the Hufnagel-Valley [21] turbulence models are frequently employed for laser propagation studies. To the best of our knowledge, however, no standard turbulence profiles exist for good astronomical sites and nighttime viewing conditions. Therefore, we have developed a modified version of the Hufnagel-Valley model that predicts a 20-cm r_0 (0.70-arc-sec seeing); this modified profile, along with a standard wind-velocity model [22], is applied in the analysis that follows. Figure 5 shows both of these functions, and Table 1 lists the associated turbulence parameters for imaging in the visible.

Estimation of Compensation-System Performance

As one might infer from the previous discussion, an adaptive optics system capable of controlling phase on spatial scales smaller than r_0 and at time intervals shorter than τ_0 provides excellent turbulence compensation. On the other hand, system complexity is a strong function of the number of degrees of freedom and the control bandwidth. Our intent in this study is to avoid design constraints that are overly stressing and have an inordinate impact on the overall system cost.

The theory and implementation of adaptive optics

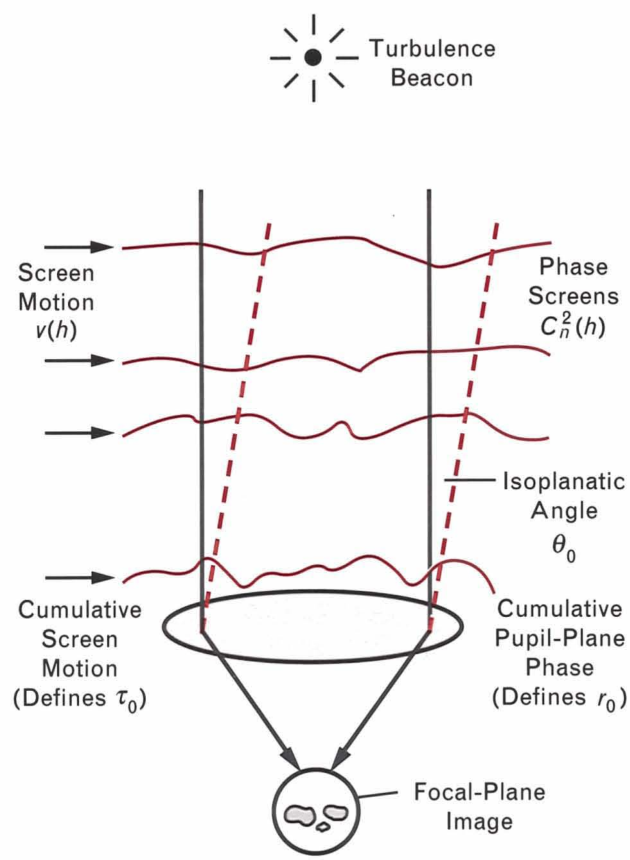

FIGURE 4. Physical processes associated with the turbulence coherence length r_0, the critical time constant τ_0, and the isoplanatic angle θ_0. The value of r_0 is related to the cumulative turbulence between the telescope and the top of the atmosphere, whereas τ_0 is a function of the average wind velocity. The value of θ_0 is determined primarily by the strength of high-altitude turbulence.

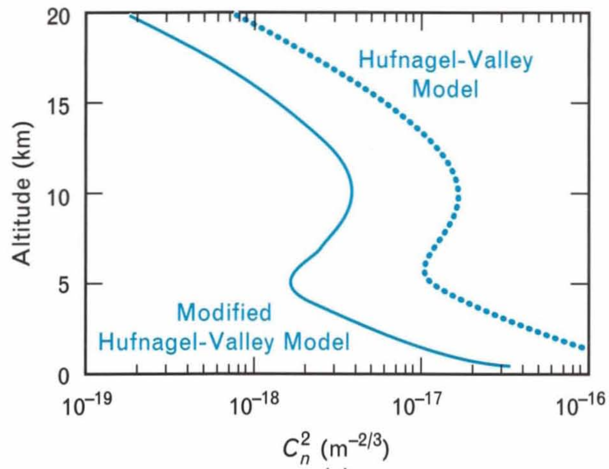

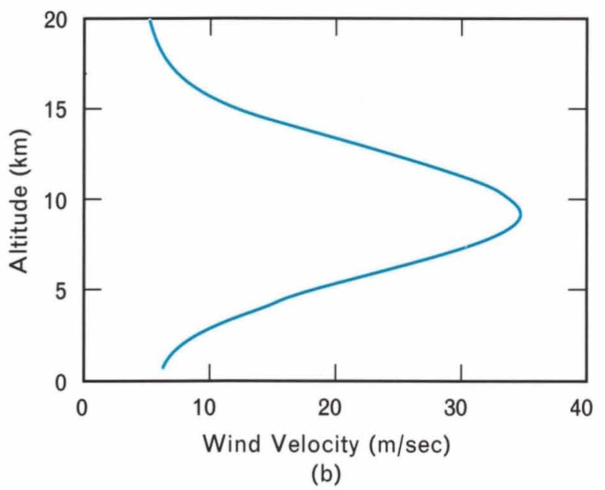

FIGURE 5. (a) Turbulence profile and (b) wind-velocity profile employed in this system study. We developed the modified Hufnagel-Valley model to represent nighttime turbulence under good seeing conditions.

systems have been investigated for at least two decades, and the basic relationships for estimating performance are well understood. The usual approach is to develop an expression for the residual pupil-plane phase error associated with each major component of the servo mechanism. These contributions are assumed to be statistically independent, so that the total error can be represented by the sum of the error variances of the individual elements:

$$\sigma^2_{\text{phase}} = \sum \sigma_i^2 .$$

This article will now describe each of the most important contributors to the total phase error.

A deformable mirror incorporates an array of independent actuators that either provides modal control (represented by a Zernike decomposition over a circular mirror [23]) or zonal control (using a rectangular matrix of elements). The latter approach has been the method of choice for high-performance correction and has been employed in all laser-beam-control systems. Under closed-loop operation a zonal mirror acts as a high-pass spatial filter that suppresses the low-frequency components of the wavefront distortion, but allows components above the Nyquist frequency to propagate to the focal plane. The resulting *fitting error* is established by the ratio between the subaperture dimension d_s and the turbulence coherence length r_0, as indicated in the following expression:

$$\sigma^2_{\text{fitting}} \approx 0.5\left(d_s/r_0\right)^{5/3} \quad (\text{rad}^2 \text{ of phase error}). \tag{2}$$

The leading constant is found to be weakly dependent on the shape of the mirror and the size of the central obscuration.

The temporal characteristics of the deformable-mirror servo system can also be described as a high-pass filter having a turbulence-rejection bandwidth β_{servo}. From the work of Greenwood [24], the follow-

Table 1. Turbulence Parameters for Viewing at 0.55 μm (Based on the Modified Hufnagel-Valley Model)

	r_0 (cm)	θ_{seeing} (arc sec)	θ_0 (μrad)	τ_0 (msec)
0° Zenith	20.0	0.69	20.0	6.3
45° Zenith	16.2	0.85	11.5	5.1

ing result is developed for the figure error due to finite servo response:

$$\sigma^2_{\text{servo}} \approx 0.96\left(\tau_d / \tau_0\right)^{5/3} \quad (\text{rad}^2 \text{ of phase error}) . \tag{3}$$

The parameter τ_d describes the dwell time of the detector array used in the wavefront sensor. In closed-loop operation, the dwell time establishes the minimum delay between the measurement of a residual distortion and the application of a correction to the deformable mirror. At high correction rates τ_d can be related to an analog servo bandwidth in the following way:

$$\beta_{\text{servo}} \approx \frac{1}{10\,\tau_d} .$$

This number is essentially equivalent to the Greenwood frequency [20] for a compensation system incorporating a sharp cutoff filter.

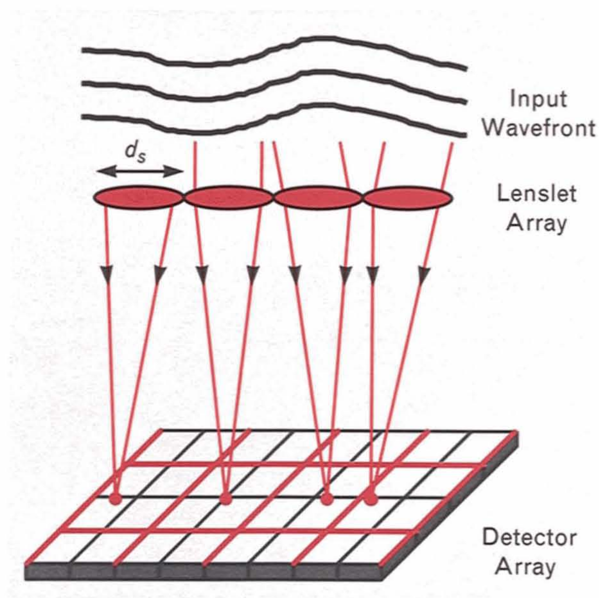

FIGURE 6. Schematic description of a Hartmann wavefront sensor. The incoming wavefront is divided into a matrix of subapertures (outlined areas) by a lenslet array, which produces a set of focused spots on a detector array. The displacement of a spot from its local null position provides a measure of the phase gradient within a subaperture.

Equations 2 and 3 address the issue of spatial and temporal resolution but not correction accuracy. For low-light-level operation this parameter is driven primarily by noise in the wavefront sensor. To address this issue, we must develop a model for the performance of the phase sensor.

At least three phase-sensing techniques have been successfully demonstrated for adaptive optics: *Hartmann sensors* in which the pupil plane is mapped into a set of lenslets that form separate images of the source [10], *shearing sensors* that convert phase gradients into intensity variations [10], and sensors that measure local wavefront curvature [25]. The Hartmann approach, illustrated in Figure 6, consists of an array of tracking devices that convert local gradients into focal-spot displacements. For this sensor the measurement error is related to the uncertainty in determining the centroid position of each spot, and includes a photon-noise component as well as a contribution from detector readout noise. For charge-coupled-device detector arrays, the measurement-error expression has the form [26]

$$\sigma^2_{\text{sensor}} \approx \underbrace{\frac{2\pi hc\left(\dfrac{k_c^2}{k_b}\right)\left[1+\left(\dfrac{k_b}{k_c}\right)^{12/5}\left(\dfrac{d_s}{r_0}\right)^2\right]}{3\eta\tau_d d_s^2 I_b}}_{\text{photon noise}} + \underbrace{\frac{2\left(hck_c\right)^2\left[1+\left(\dfrac{k_b}{k_c}\right)^{12/5}\left(\dfrac{d_s}{r_0}\right)^2\right]N_{rms}^2}{3\left(G_e\eta\tau_d d_s^2 I_b\right)^2}}_{\text{detector noise}} , \tag{4}$$

where the following definitions apply: $k_c = 2\pi/\lambda$ is the center wave number of the imaged light, $k_b = 2\pi/\lambda_b$ is the beacon wave number, ζ is the zenith angle, h is the detector quantum efficiency at the beacon wavelength, N_{rms} is the detector transfer noise, G_e is the gain of the optical intensifier, τ_d is the phase-sensor dwell time, d_s is the subaperture diameter, and I_b is the pupil-plane irradiance from the beacon.

The quantity in square brackets in the numerator of both noise terms in Equation 4 represents a correction factor that describes the loss in measurement sensitivity when the subaperture dimension exceeds the turbulence coherence length. For imaging applications in which modest performance gains are acceptable, we can simplify Equation 4 by assuming that the subaperture diameter is larger than r_0. Under high readout-rate operation the sensor is likely to be detector-noise limited, so that the following expression for measurement error is appropriate:

$$\sigma^2_{\text{sensor}} \approx \frac{2(hc)^2 k_b^{12/5} k_c^{-2/5} N^2_{rms}}{3(\eta \tau_d r_0 d_s I_b)^2} \quad (5)$$

$$(\text{rad}^2 \text{ of phase error}).$$

The sum of the variances given by Equations 2, 3, and 5 forms the basis of a performance expression in which a decrease in d_s and τ_d improves the measurement resolution (by reducing the fitting and finite-bandwidth errors, respectively) but increases the sensor error. This relation suggests a design-optimization strategy in which the system parameters are adjusted to minimize the required beacon irradiance I_b for a fixed level of error. Figure 7 shows an example of this optimization process for a compensation system operating at visible wavelengths. To facilitate comparisons with other astronomical instruments, we represent the aperture irradiance I_b in terms of equivalent stellar magnitude m_v through the relationship

$$m_v \approx -2.5\log(I_b/\gamma_r) - 21.2,$$

where γ_r is the total throughput of the atmosphere and the receiver optics. In this example (and in subsequent calculations) γ_r is assumed to be 20%.

Characterization of Focal-Plane Image Quality

The process illustrated in Figure 7 provides a mechanism for selecting an appropriate set of design parameters once the allowable phase distortion has been established, but it provides no guidance to the appropriate level of performance for compensated-imaging applications. To address this question we must investigate the relationship between pupil-plane phase error and focal-plane image quality.

A high-performance beam-control system is frequently characterized by the Strehl ratio, which defines the ratio between the achieved on-axis beam intensity and the diffraction-limited value. When the residual phase distortion σ^2_{phase} is less than 1 rad^2, the extended Maréchal approximation,

$$\text{Strehl} \approx \exp\left(-\sigma^2_{\text{phase}}\right),$$

gives an accurate estimate of the Strehl. This relationship, however, provides no information about the

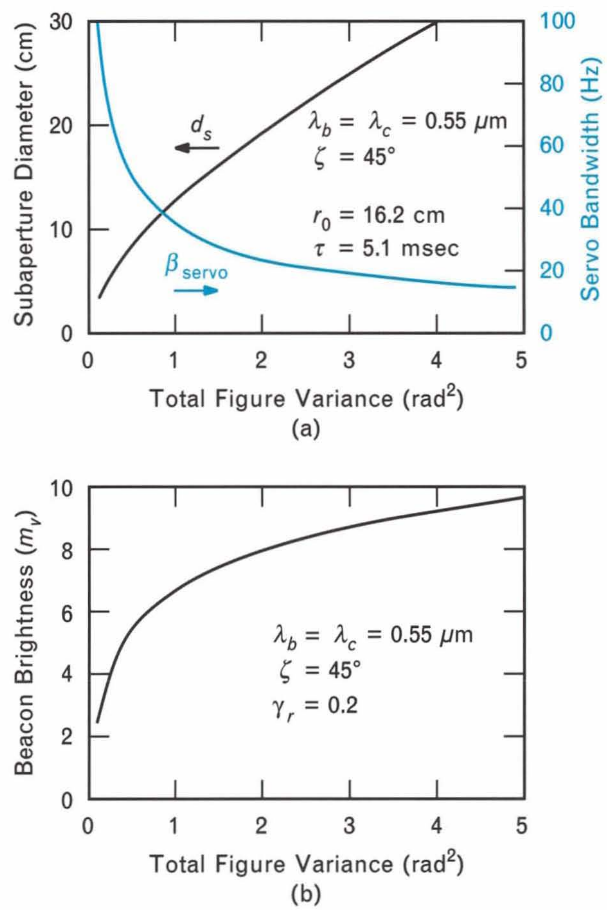

FIGURE 7. Design space for an optimization procedure that (a) adjusts the subaperture diameter and servo bandwidth to (b) minimize the beacon irradiance needed to achieve a given pupil-plane phase distortion. We assume that the error variance is evenly divided between fitting error, servo error, and wavefront-sensor noise. Beacon brightness is given in terms of visual magnitude for a receiver throughput (including optics and atmosphere) of 20%. These results are independent of aperture diameter.

shape of the far-field image.

The proper study of imaging systems incorporating partial turbulence compensation requires a more detailed characterization of the focal-plane energy distribution. For convenience we divide the residual phase into a tracking error σ_{tilt}^2 (rad^2 of single-axis tilt jitter) associated with the tilt-control element and a figure error σ_{figure}^2 (rad^2 of phase) associated with the high-spatial-frequency correction applied by the deformable mirror.

The instantaneous (or short-exposure) image of an object viewed through turbulence consists of a diffraction-limited primary lobe and an array of sidelobes covering a region of diameter λ / r_0. The ratio between the primary and sidelobe energies depends on the magnitude of σ_{figure}^2. In a long-exposure image the randomly fluctuating sidelobes average to form a smooth background skirt, and the entire profile is broadened by uncorrected beam motion. The net result is a point-spread function that can be described as the sum of two quasi-Gaussian shapes determined by the ratio of the wavelength and aperture diameter λ / D, the ratio of the wavelength and turbulence coherence length λ / r_0, and the long-exposure image jitter σ_{tilt}. These concepts are illustrated in Figure 8.

If we apply the Maréchal approximation to describe the central core of the beam and assume that energy lost from the core is contained in the background skirt, then we obtain the following empirical expression for the long-exposure Strehl:

$$[\text{Strehl}]_{\text{LE}} \approx \underbrace{\frac{\exp\left(-\sigma_{\text{figure}}^2\right)}{1 + 4.94\left(\dfrac{D}{\lambda}\right)^2 \sigma_{\text{tilt}}^2}}_{\text{central core}} + \underbrace{\frac{1 - \exp\left(-\sigma_{\text{figure}}^2\right)}{1 + \left(\dfrac{D}{r_0}\right)^2}}_{\text{background}} .$$

This description gives the expected value for all limiting values of the figure and tilt variance, and is in good agreement with computer-simulation results.

A definition of the effective angular resolution is somewhat less obvious, but an expression incorporating the weighted rms of the central core and background diameters provides a plausible first-order estimate of this parameter:

$$[\text{Resolution}]_{\text{LE}} \approx 1.22\left(\frac{\lambda}{D}\right)\frac{\alpha}{[\text{Strehl}]_{\text{LE}}}, \text{ where}$$

$$\alpha = \sqrt{\frac{\exp\left(-2\sigma_{\text{figure}}^2\right)}{1 + 4.94\left(\dfrac{D}{\lambda}\right)^2 \sigma_{\text{tilt}}^2} + \frac{\left[1 - \exp\left(-\sigma_{\text{figure}}^2\right)\right]^2}{1 + \left(\dfrac{D}{r_0}\right)^2}} . \tag{6}$$

Equation 6 predicts a rapid transition from the diffraction limit to the uncompensated-resolution limit when the figure error exceeds a critical value that depends on the ratio D / r_0. Figure 9 illustrates this

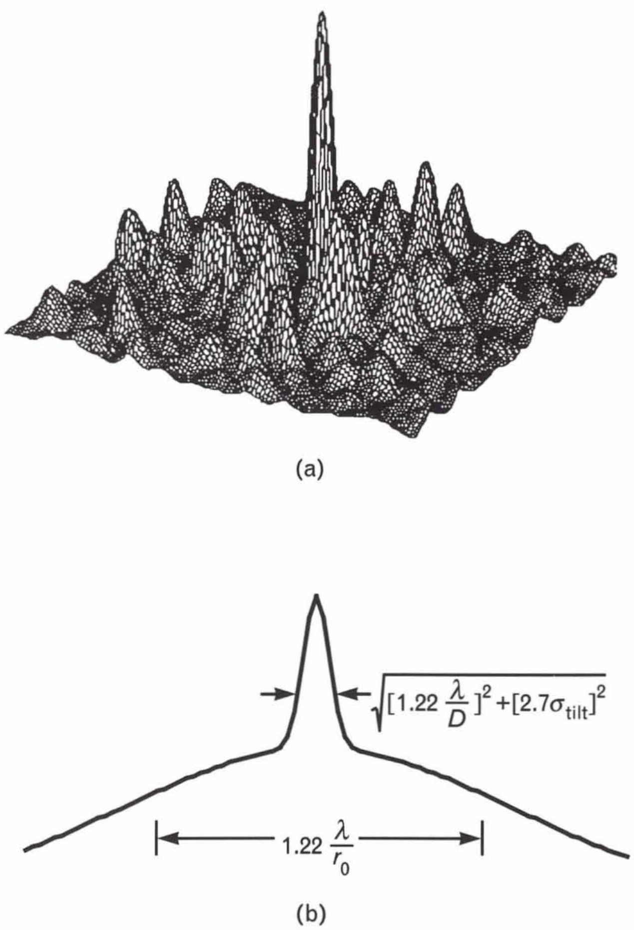

FIGURE 8. (a) The short-exposure image of a point source viewed through turbulence is characterized by a diffraction-limited central core and an array of sidelobes. (b) In the long-exposure profile the sidelobes are averaged to form a smooth skirt, and the entire beam is broadened by image motion.

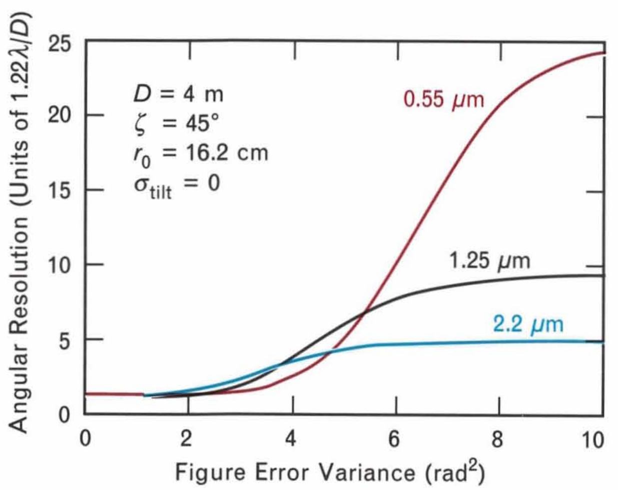

FIGURE 9. Resolution as a function of pupil-plane phase distortion level for partially corrected turbulence (tracking error has been ignored). The point of transition from diffraction-limited to uncorrected turbulence depends on the D/r_0 ratio. For the wavelengths of interest this transition begins in the range of 2 to 4 rad^2.

behavior for a 4-m system that is assumed to have no tracking error.

For the imaging wavelengths of interest (visible and near-infrared), the effective resolution is seen to be near diffraction-limited as long as σ^2_{figure} is less than 3 rad^2. From Figure 7 we see that this restriction on figure error implies the following constraints on the subaperture size and servo bandwidth:

$$d_s < 1.5\, r_0 \text{ and } \beta_{\text{servo}} > \frac{1}{10\,\tau_0}\ .$$

This level of performance also requires a star of magnitude 8 or brighter for imaging in the visible. The possibility of using as a beacon a bright neighboring star within the isoplanatic angle of a dim object will be introduced later, in a section in which fractional sky coverage is addressed.

Laser Guide Stars for Dim-Object Astronomy

Laser guide stars (or synthetic beacons), created by the backscatter of intense laser beams, offer a viable means to extend the utility of adaptive optics to dim objects. The feasibility of this technique has been clearly demonstrated in several recent experiments [14, 18, 19]; we now discuss its application to large astronomical systems.

Single-Beacon Geometries

Figure 10 indicates how light rays originating from a distant source propagate along parallel lines to the receiver aperture, whereas those from a synthetic beacon diverge from a scattering volume at a finite focal distance. The measurement of accumulated phase distortion afforded by a laser guide star is thus inherently imperfect because of unsampled turbulence above the beacon and incorrectly sampled turbulence below the beacon. This form of error is referred to as focal anisoplanatism because it results from a difference in range between the beacon and the more distant target object.

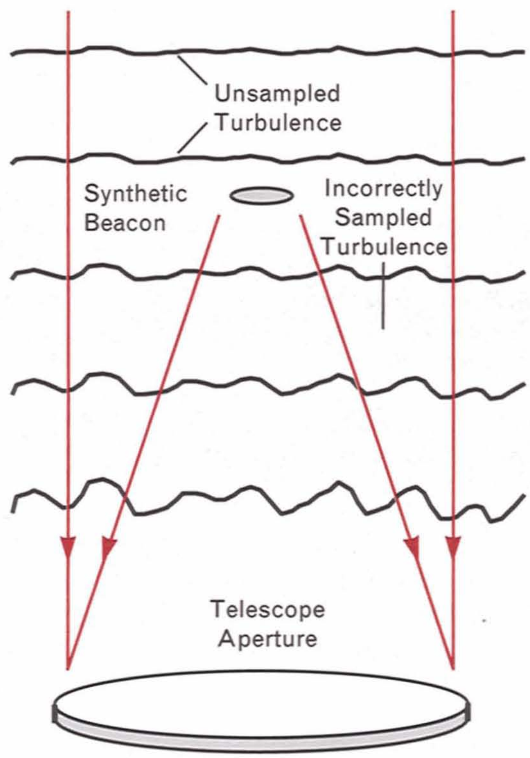

FIGURE 10. The two sources of phase error introduced by synthetic beacons. The vertical rays represent light originating from a distant source; this light accumulates phase error in traveling through the atmosphere to the telescope. Radiation from the laser guide star follows a slightly different path to the telescope and is therefore unable to sample turbulence distortions above the beacon altitude or to sample accurately the turbulence that lies below the beacon.

Focal anisoplanatism can be reduced by using backscattered light from a higher altitude or by using multiple beacons. Because this effect plays a central role in the performance of laser guide-star compensated-imaging systems, we begin our discussion with an estimate of the magnitude of this error.

By using an analytical technique recently developed by R.J. Sasiela [27] that applies Mellin transform theory to complicated turbulence calculations, we can describe a wide range of atmospheric effects in terms of expansions involving turbulence moments (introduced earlier in this article). Following Sasiela, the anisoplanatic errors associated with a beacon located at altitude H are

$$\sigma^2_{\text{upper}} \approx 0.057 D^{5/3} k_c^2 \sec(\zeta) \mu_0^{\uparrow}(H)$$

and

$$\sigma^2_{\text{lower}} \approx D^{5/3} k_c^2 \sec(\zeta) \times \left\{ 0.50 \frac{\mu^{\downarrow}_{5/3}(H)}{H^{5/3}} - 0.45 \frac{\mu^{\downarrow}_{2}(H)}{H^2} + \cdots \right\}, \tag{7}$$

where the notations

$$\mu_n^{\downarrow}(H) = \int_0^H h^n C_n^2(h)\, dh$$

and

$$\mu_n^{\uparrow}(H) = \int_H^\infty h^n C_n^2(h)\, dh$$

represent the lower and upper partial moments, respectively. These equations exhibit a strong dependence on H, which indicates that it is advantageous to place the beacon at the highest practicable altitude.

The maximum useful beacon range is ultimately limited by the transmitted laser power and the physics of the scattering phenomenon. The return from low altitudes is dominated by Rayleigh scattering, which decreases rapidly with range as a result of the reduction in the solid angle subtended by the collector and the decrease in molecular density at higher altitudes. The aperture irradiance I_b is governed by the expression

$$I_b \approx P_l \frac{\gamma_t \gamma_r n(H) [d\sigma(\pi)/d\Omega] \Delta R}{[\sec(\zeta) H]^2},$$

where P_l is the average laser power, γ_t is the total uplink transmission (including atmospheric losses), γ_r is the total downlink transmission (including atmospheric losses), $n(H)$ is the molecular density, $d\sigma(\pi)/d\Omega$ is the backscatter cross section, and ΔR is the wavefront-sensor range gate. Because the cross section for Rayleigh backscatter varies as λ^{-4}, there is strong motivation to operate with short-wavelength sources.

As a source of light for an adaptive optics wavefront sensor, Rayleigh scattering is impractical from altitudes beyond 20 km. Fortunately, the earth's mesosphere contains a high concentration of sodium formed by meteorite collisions with the outer atmosphere, and these atoms exhibit a strong resonant backscatter at 0.589 μm. The cross section for this effect is large (6.6×10^{-17} m^2/sr) compared to the cross section for Rayleigh backscatter (4.1×10^{-32} m^2/sr at 0.589 μm). If saturation of the sodium molecules is ignored, a first-order estimate of the aperture irradiance can be written as

$$I_b \approx P_l \frac{\gamma_t \gamma_r C_s [d\sigma(\pi)/d\Omega]}{[\sec(\zeta) H_s]^2},$$

where H_s = 90 km is the altitude of the sodium layer

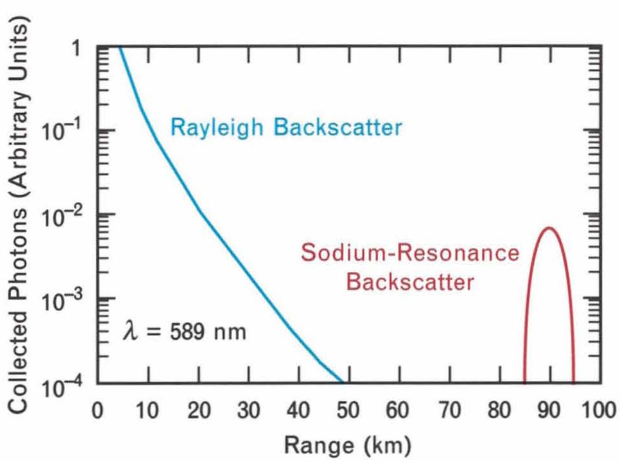

FIGURE 11. Comparison of Rayleigh backscatter and sodium-resonance backscatter as a function of beacon altitude for a propagation wavelength of 0.589 μm.

and $C_s \approx 5 \times 10^{13}$ atoms/m^2 is the range-integrated sodium column abundance. Figure 11 shows a qualitative comparison of laser-beam return as a function of altitude for 0.589-μm radiation.

Multiple-Beacon Concepts

An alternative to the deployment of a high-altitude beacon is the use of an array of sources, each of which provides phase information to a single segment of the full aperture. The benefit of this approach is that the average sampling path more nearly matches the parallel rays from the target object. Equation 7 suggests that, by partitioning the aperture into sections of diameter D_s, we can reduce the error due to the low-altitude component of focal anisoplanatism by a factor of $(D_s/D)^{5/3}$. (Increasing the number of beacons, however, does not improve the error due to the unsampled turbulence above the beacon altitude.)

The idea of deploying multiple sources for large-aperture compensation is nearly as old as the original single-beacon concept, and it has received extensive attention from theorists in the past several years. The practical implementation of this scheme is far from trivial, however, and the following issues are noted. First, the return radiation from each beacon must carry a unique identifying characteristic, such as time of arrival, color, polarization, or field of view, so that measurements made by the wavefront sensor can be correctly processed. Second, because wavefront sensors measure phase gradients rather than absolute phase, a means must be found to measure gradients across the seams between the aperture sections. To accomplish this *stitching* process, the detectors at the edges of the sections must be capable of measuring light from both of the neighboring sources. Third, the process of combining gradient data from multiple sources leads to an irreducible measurement noise, referred to as *stitching error*, that partially offsets the elimination of low-altitude focal anisoplanatism.

Stitching error arises from the need to combine gradient measurements from many sources whose relative positions cannot be precisely controlled (see the box entitled "Multiple-Beacon Section Stitching"). This effect can be minimized by subtracting the aperture-average tilt from each set of measurements prior to subsequent processing. This renormalization, however, renders the system insensitive to spatial frequencies corresponding to the beacon spacing. The resulting error function is only weakly dependent on the number of beacons deployed, and has the approximate form [26]

$$\sigma^2_{\text{stitching}} \approx D^{5/3}\, k_c^2 \sec(\zeta)\left\{0.040\,\frac{\mu_2^{\downarrow}(H)}{H^2} + \cdots\right\}.$$

Figure 12 compares our estimates of the magnitude of focal anisoplanatism for the single-beacon

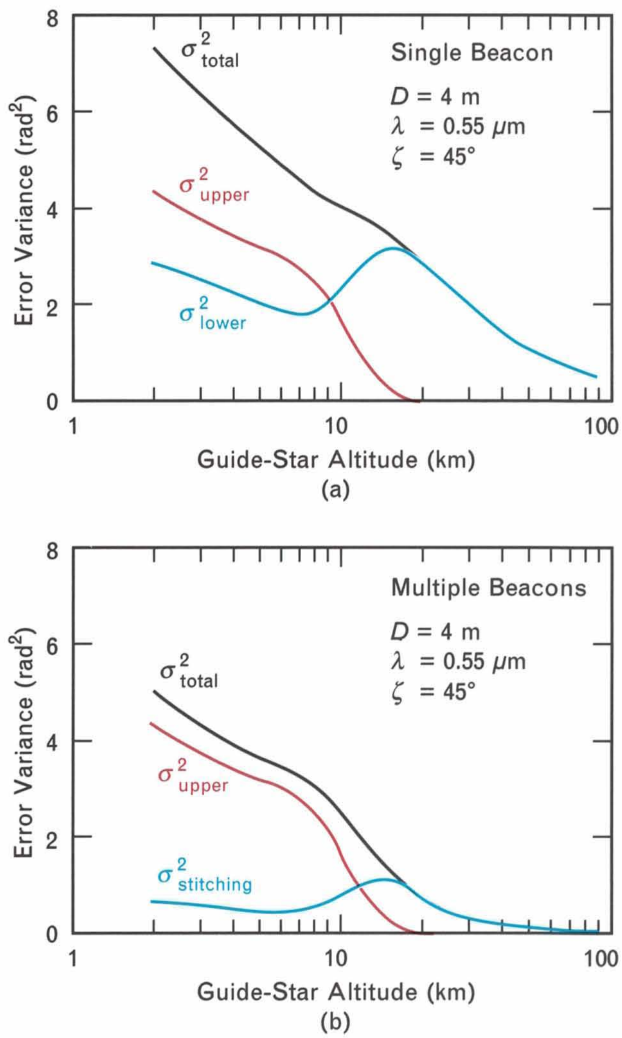

FIGURE 12. Comparison of focal-anisoplanatic errors for (a) single-beacon performance and (b) multiple-beacon systems as a function of beacon altitude. To maintain good image quality the total error due to this effect should be kept below 1 rad^2. This goal can be achieved with several beacons (on the order of 8) at 20 km or a single beacon at 90 km.

MULTIPLE-BEACON SECTION STITCHING

THE DEPLOYMENT OF a large number of synthetic beacons decreases the diameter of the aperture section that receives light from any one source, which makes the backscattered rays more parallel so that measurement errors due to focal anisoplanatism are reduced. When the beacon array is propagated upward through the atmosphere, however, the relative source positions exhibit random fluctuations because of jitter in the projection system and differences in the integrated turbulence paths (see Figure A). If uncorrected, these lateral displacements are interpreted as low-spatial-frequency tilts by the wavefront sensor.

Because there is no way to distinguish between a physical distortion of the beacon matrix and apparent displacements caused by turbulence, errors resulting from the process of combining, or *stitching,* information received from multiple sources can be minimized by eliminating nonzero average-tilt components from the collected data. This nulling process can only be performed in a relative sense, and it requires some degree of measurement overlap between adjacent aperture sections. Stitching is best performed if all subapertures can sense the

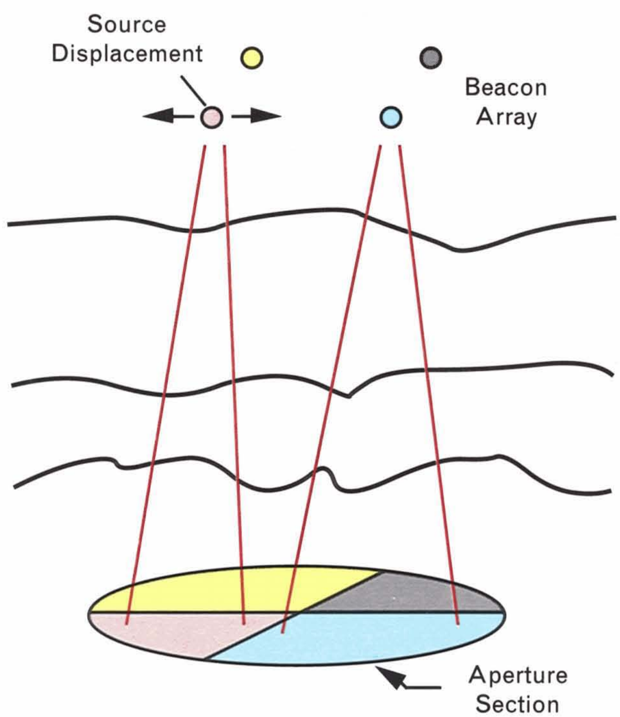

FIGURE A. Any movement of an individual beacon within a multiple-source array imposes a differential tilt component on all of the gradient measurements associated with that section. The result is a low-spatial-frequency distortion of the reconstructed wavefront.

and multiple-beacon geometries. As explained earlier, the use of a single source at a finite range gives rise to a high-altitude error representing unsampled turbulence and a low-altitude error related to the incorrect sampling of turbulence below the beacon. If a sufficient number of Rayleigh sources are deployed (approximately 1 per m^2 for visible imaging), the low-altitude anisoplanatic error component becomes negligible but is replaced by stitching error.

To put these results into perspective, recall that we previously developed an error budget based on a maximum pupil-plane phase variance of 3 rad^2. The contribution due to focal anisoplanatism should be kept below 1 rad^2 to maintain a reasonable balance between the various sources of compensation error. For visible imaging with a 4-m telescope, Figure 12 indi-

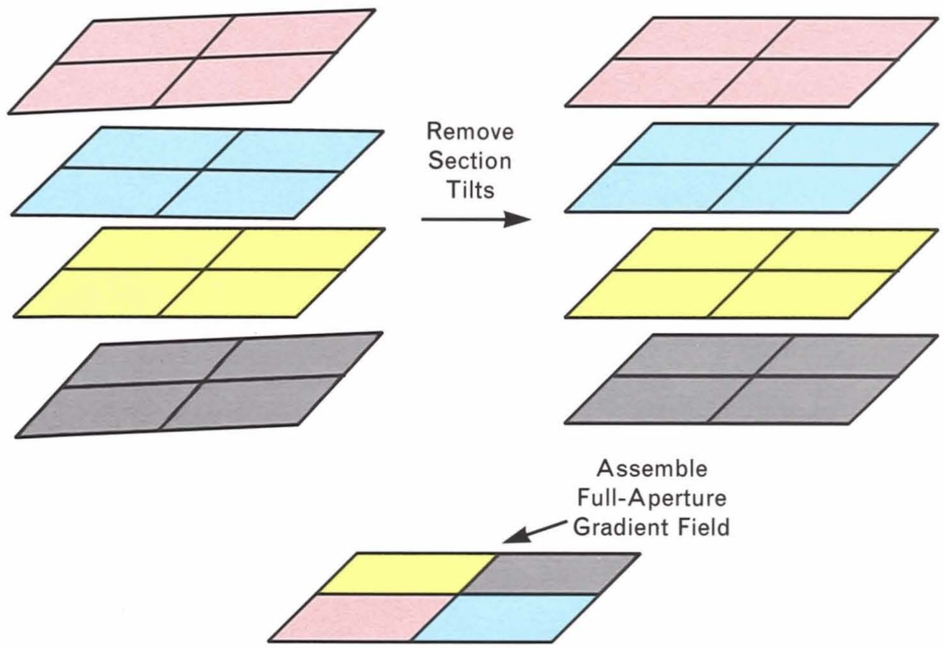

FIGURE B. The aperture-average tilt must first be removed from each data ensemble to eliminate the possibility of introducing anomalous tilt components into the reconstruction process. Gradients can then be selected from the field associated with the nearest beacon.

light from all of the deployed beacons.

Although optimal estimation can be applied to this reconstruction process, good results can be achieved with a simple two-step algorithm in which the full-aperture tilt is first subtracted from each gradient sample. Local gradients derived from the source closest to each subaperture are then input to the computational device that forms a least-squares estimate of the wavefront (see Figure B). The error incurred as a result of losing low-spatial-frequency information is known as *stitching error.*

cates that this goal can be met with either one sodium beacon at 90 km or several (of order 8) Rayleigh sources at 20 km. Because of the practical difficulties associated with the deployment of multiple probes, we are currently focusing on the development of lasers that operate at the sodium-resonance frequency.

Estimation of Sky Coverage

One might conclude from the preceding discussion that only stars brighter than 8th magnitude can be compensated directly, but that synthetic beacons can be used to apply high-quality phase correction to any celestial body; neither of these statements is correct. Direct compensation can be applied to a dim object if it lies close enough to a star that is sufficiently bright to drive the wavefront sensor. Furthermore, as we will show, synthetic-beacon compensation requires a nearby tracking source for image stablization. The probability that a suitable star can be located for these purposes establishes the system's overall functionality, or fractional sky coverage.

Off-Axis Phase Correction for Natural-Star Systems

Equation 1 introduced the concept of an isoplanatic angle within which a fixed beacon provides valid phase information. A quantitative estimate of the residual phase error that results when the beacon and object under observation are separated by an angle θ is given by [28]

$$\sigma^2_{\text{offset}} \approx \left(\theta/\theta_0\right)^{5/3} \quad (\text{rad}^2 \text{ of phase error}). \qquad (8)$$

This form of error is known as *offset anisoplanatism.* At visible wavelengths the isoplanatic angle θ_0 is typically of the order of a few arc seconds.

Offset anisoplanatism represents the fourth term in the budget for figure error:

$$\sigma^2_{\text{figure}} = \sigma^2_{\text{fitting}} + \sigma^2_{\text{servo}} + \sigma^2_{\text{sensor}} + \sigma^2_{\text{offset}}. \qquad (9)$$

Because this compensation scenario assumes that a beacon star is close to the target object and bright enough to drive the wavefront sensor, tracking jitter is negligible:

$$\sigma^2_{\text{tilt}} \approx 0. \qquad (10)$$

The probability of locating a star of sufficient brightness within the isoplanatic patch of the viewing direction can be derived from standard tables listing the number of stars versus visual magnitude [29]; these data were used to generate the star-density curves shown in Figure 13. The average star density is accurately approximated by an exponential function of the visual magnitude:

$$\text{average density} \approx 1.45 \exp(0.96\, m_v) \quad (\text{stars / rad}^2). \qquad (11)$$

From Equations 8 and 11, we obtain an estimate of the fractional sky coverage associated with an isoplanatic error of magnitude σ^2_{offset}:

$$\begin{aligned} &\text{fractional sky coverage} \approx \\ &\pi\,\theta^2 \times \text{average density} \approx \\ &4.6 \exp(0.96\, m_v)\, \theta_0^2 \left(\sigma^2_{\text{offset}}\right)^{6/5} \end{aligned} \qquad (12)$$

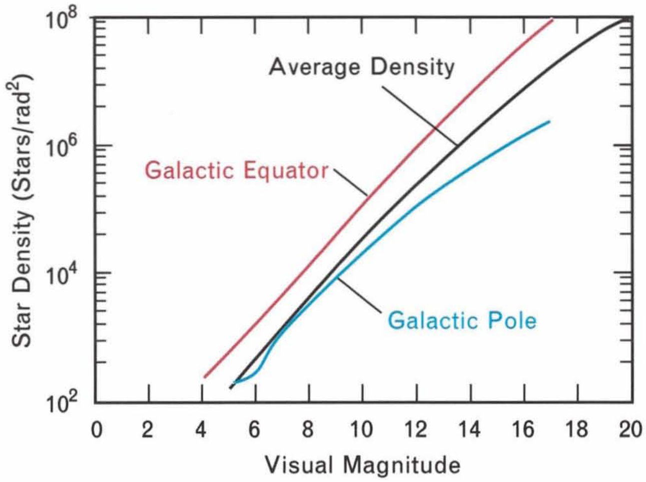

FIGURE 13. Comparison of stellar densities for the galactic pole, galactic equator, and global average as a function of visual magnitude (from Reference 29).

Equations 9, 10, and 12 represent a complete description of the performance and utility of a compensated-imaging system that uses natural-star beacons. Because performance and utility share an inverse relationship, we must take care to develop a design methodology that suits the particular imaging application. A reasonable first-order approach, which leads to an unambiguous specification of all parameters, is to identify a maximum allowable figure error that is evenly divided among the four terms in Equation 9. For the baseline turbulence parameters given in Table 1, the predicted fractional sky coverage for visible imaging is of the order of 10^{-6}. Although useful science can be performed even if our access to the sky is limited, the real potential of adaptive optics is achievable only with the use of synthetic-beacon sources.

Off-Axis Tilt Stabilization for Synthetic-Beacon Systems

Perhaps the most important issue associated with the practical application of synthetic beacons to astronomy is the need to establish a tracking source for long-exposure data collection. Tilt information cannot be obtained from laser backscatter because the beam follows the same optical path in both the outgoing and return directions. Unless turbulence-induced image motion can be sensed and eliminated, the figure compensation afforded by the deformable-mirror subsystem is of little value. Currently, the only practical solution to this problem is to locate a nearby reference star that is bright enough to drive a separate tracking system.

A performance analysis of a null-seeking tracker obtains directly from the earlier discussion of Hartmann phase sensors. Because each Hartmann subaperture is a complete tracking unit, the associated angular error over an aperture of diameter D can be derived from Equation 4 by multiplying the measurement error by $4/\pi(k_c D)^2$. To allow for the possibility that the beacon and tracking wavelengths may differ, the parameters k_t, τ_{dt}, and I_t are introduced to represent the tracker wave number, sensor dwell time, and pupil-plane irradiance, respectively. Finally, we assume that the full aperture is much larger than r_0 and that photon-noise-limited operation can be obtained with a low-bandwidth quad-cell detector. With these modifications, the expression for tracking error due to measurement noise becomes

$$\left(\sigma^2_{\text{sensor}}\right)_{\text{tilt}} \approx \frac{8 h\, c\, k_c^{-12/5}\, k_t^{7/5}}{3 \eta\, \tau_{dt}\, r_0^2 D^2 I_t}$$
$$(\text{rad}^2 \text{ of tilt error}),$$

which is independent of aperture diameter when normalized to the diffraction-limited beamwidth.

The tracking error associated with a finite dwell time depends quadratically on the ratio of the tracker integration period and the atmospheric time constant [26]

$$\left(\sigma^2_{\text{servo}}\right)_{\text{tilt}} \approx 0.20 \left(\frac{\lambda_c}{D}\right)^2 \left[\frac{\tau_{dt}}{\left(\tau_0\right)_{\text{tilt}}}\right]^2$$
$$(\text{rad}^2 \text{ of tilt error}).$$

The characteristic time constant $\left(\tau_0\right)_{\text{tilt}}$ for tilt derives from a temporal-frequency model having an $f^{-2/3}$ dependence at low frequencies, and a magnitude that includes the velocity moment $v_{-1/3}$ [30]. A first-order calculation of this parameter produces the expression

$$\left(\tau_0\right)_{\text{tilt}} = \left\{0.51\, k_c^2 \sec(\zeta)\, v_{-1/3}^{8/15}\, v_{14/3}^{7/15}\, D^{-1/3}\right\}^{-1/2},$$

which is seen to be weakly dependent on the aperture diameter. This number is typically a factor of two or three larger than the time constant for figure compensation.

The third factor affecting tracker performance is the anisoplanatic error associated with an angular displacement between the target object and the fiducial reference. Here again we find a quadratic dependence on the primary variable [26],

$$\left(\sigma^2_{\text{offset}}\right)_{\text{tilt}} \approx 0.20 \left(\frac{\lambda_c}{D}\right)^2 \left[\frac{\theta}{\left(\theta_0\right)_{\text{tilt}}}\right]^2 \tag{13}$$
$$(\text{rad}^2 \text{ of tilt error}),$$

where

$$\left(\theta_0\right)_{\text{tilt}} = \left\{0.67\, k_c^2 \sec^3(\zeta)\, \mu_2\, D^{-1/3}\right\}^{-1/2}$$

is the tilt isoplanatic angle. At visible wavelengths $\left(\theta_0\right)_{\text{tilt}}$ is approximately 8 arc sec, which is about four times larger than θ_0.

A total of seven major components is needed to specify the performance of a laser guide-star system, four of which relate to figure error,

$$\sigma^2_{\text{figure}} = \sigma^2_{\text{fitting}} + \sigma^2_{\text{servo}} + \sigma^2_{\text{sensor}} + \sigma^2_{\text{focus}},$$

and three that describe tracking fluctuations,

$$\sigma^2_{\text{tilt}} = \left(\sigma^2_{\text{servo}}\right)_{\text{tilt}} + \left(\sigma^2_{\text{sensor}}\right)_{\text{tilt}} + \left(\sigma^2_{\text{offset}}\right)_{\text{tilt}}. \tag{14}$$

The equation for sky coverage derives from Equations 11 and 13, which yield an expression that is directly related to the allowable tracking error:

fractional sky coverage ≈

$$22.8 \exp\left(0.96\, m_v\right)\left(\theta_0\right)^2_{\text{tilt}} \left(\frac{D}{\lambda_c}\right)^2 \left(\sigma^2_{\text{offset}}\right)_{\text{tilt}}.$$

If we follow the same design strategy used previously and divide the total tilt error among the terms listed in Equation 14, then a relationship can be developed

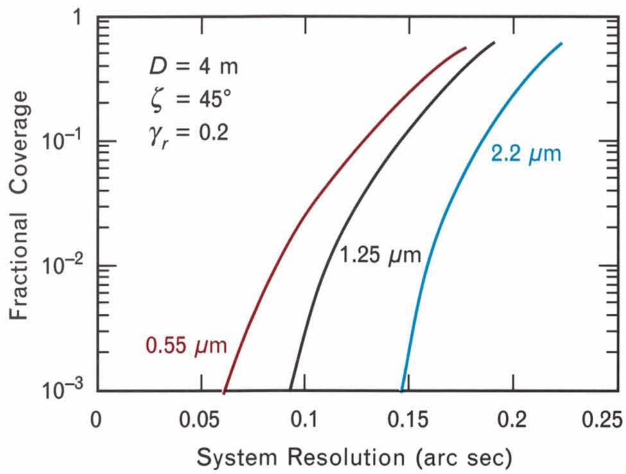

FIGURE 14. The fraction of the sky over which a given resolution can be attained for a laser guide-star compensated-imaging system. Effects of residual image motion due to finite tracker bandwidth, limited signal, and offset anisoplanatism are included. The uncorrected seeing at 0.55 μm is 0.85 arc sec for the atmospheric conditions used in this study.

between the limiting system resolution for good phase correction ($\sigma^2_{\text{figure}} < 3\ \text{rad}^2$) and the probability that a suitable reference star can be located. Because of the large isoplanatic angle for tilt and the ability of the tracking system to work with relatively dim fiducial stars, substantial gains in the effective resolution can be obtained with high probability. Figure 14 shows that the density of high-brightness stars is sufficient to improve seeing by a factor of four over the entire sky.

Comparison of Adaptive Optics Constructs for Astronomical Applications

We have now developed all of the relationships needed to design an adaptive optics system for astronomy, and we can proceed to estimate overall performance for various configurations. For the sake of discussion we assume that important scientific advances can be achieved if the central core of the long-exposure point-spread function is at least 10 times as intense as the residual background skirt. When using a synthetic beacon we must also specify the maximum acceptable tracking jitter, and we allow image motion to increase the width of the central core by no more than twice the diffraction limit. These criteria are, of course, arbitrary; the actual choice depends on the specific goals of the observation. Given another set of standards, however, the analysis would follow the same general path as that presented here. Table 2 reviews the system and turbulence parameters that have been applied in this study, and Figure 15 illustrates the beam-profile criteria.

Table 2. System Parameters for Baseline Calculations

Aperture diameter	$D = 4$ m
Beacon wavelength	$\lambda_b = 0.589\ \mu$m
Zenith angle	$\zeta = 45°$
System throughput	$\gamma_t = \gamma_r = 0.2$
Detector quantum efficiency	$\eta = 0.8$
Detector noise level	$N_{rms} = 20$
Turbulence parameters for imaging at 0.55 μm	$r_0 = 16$ cm $\theta_0 = 12\ \mu$rad $\tau_0 = 5$ msec $(\theta_0)_{\text{tilt}} = 40\ \mu$rad $(\tau_0)_{\text{tilt}} = 12$ msec

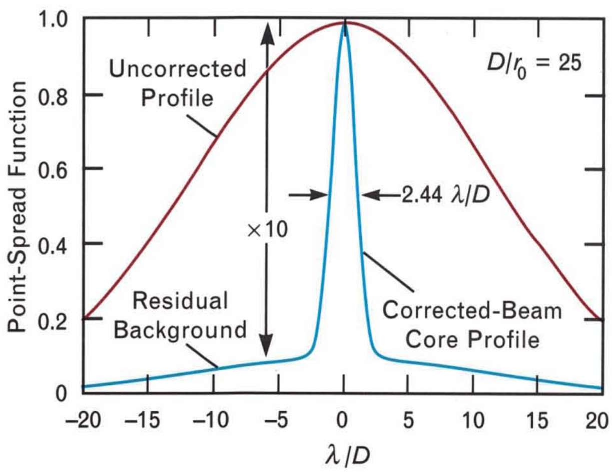

FIGURE 15. Comparison of the corrected and uncorrected beam profiles for a design criterion that restricts the image motion to twice the diffraction-limited beam diameter and achieves a signal-to-background ratio of 10. This example is representative of a 4-m system operating at 0.55 μm.

Table 3 summarizes the performance of a set of 4-m adaptive optics systems that have been optimized for either natural-star or synthetic-beacon compensation and for operation in one of three spectral wavebands. As discussed earlier, the optimization procedure incorporates an error budget in which the allowable figure and tilt errors are evenly apportioned among the major sources of degradation.

The left side of Table 3 lists the design parameters and overall performance of systems that use natural stars close to the target object to measure both the figure and tilt components of turbulence. The right side of the table refers to designs that employ a single sodium-resonance beacon to extract figure information but rely on natural stars for image stabilization. The performance results indicate that, with adaptive optics, substantial gains in both Strehl ratio and resolution can be achieved for visible and near-infrared astronomy. Although the designs become progressively easier to accomplish at longer wavelengths, all of these systems are within the state of the art. The most stressing parameter is the requisite laser power, but we note that a 20-W flashlamp-pumped solid

Table 3. 4-m System Performance Summary

	Natural-Star System			*Synthetic-Beacon System*		
	V Band 0.55 μm	J Band 1.25 μm	K Band 2.2 μm	V Band 0.55 μm	J Band 1.25 μm	K Band 2.2 μm
Number of actuators	290	85	45	250	90	65
Servo bandwidth (Hz)	23	12	9	21	12	11
Average laser power (W)	—	—	—	47	9	6
Star brightness (m_v)[1]	8	10	11	13	16	18
Strehl ratio	0.016	0.11	0.32	0.015	0.082	0.17
Resolution ($\times$ 1.22 λ/D)	2.6	1.3	1.0	3.1	2.0	2.0
Fractional sky coverage	3×10^{-6}	7×10^{-5}	3×10^{-4}	0.003	0.2	1
Number of stars (direct observation)	4×10^4	3×10^5	7×10^5	5×10^6	9×10^7	6×10^8

[1]Star brightness refers to the requirement on the neighboring source that provides wavefront-sensor illumination for the synthetic-beacon system.

state laser operating at 0.589 μm has been built at Lincoln Laboratory [31, 32], and a design exists for a diode-pumped system that will deliver approximately 200 W of average power.

The fourth row of Table 3, which indicates the motivation for using synthetic beacons, presents estimates of the star brightness required for either figure or tilt correction. Full-aperture tracking can be performed with a source that is approximately six visual magnitudes dimmer than that needed to obtain high-spatial-frequency phase information; this difference translates into an improvement factor of over 1000 in the fractional sky coverage. At infrared wavelengths the profile criteria given in Figure 15 can be achieved over virtually the entire sky. Furthermore, more advanced techniques, such as the use of a separate adaptive optics system for the tracking star, may make it possible to achieve complete sky coverage in the visible as well.

Conclusions

At this point there is little doubt as to the applicability of adaptive optics to the field of astronomy. Experiments conducted by researchers at Lincoln Laboratory and other facilities have conclusively demonstrated the efficacy of both the wavefront-compensation technology and the laser guide-star concept. Much still needs to be done, however, before adaptive optics technology is widely accepted as a tool for astronomical research. Most of the work performed to date in the field of turbulence compensation has been directed toward military problems in which the achievement of near-unity Strehl ratios has been the primary goal. Effectively adapting this technology to astronomical telescopes will require an emphasis on reducing overall system complexity and cost while maintaining component reliability. The first step in this process is to establish acceptable criteria for astronomical performance, upon which a suitable balance between capability and design sophistication can be achieved. This issue has been our principal motivation in the analysis just presented.

Acknowledgments

This work is the culmination of a lengthy investigation, during which the assistance of several individuals has been invaluable. I am particularly indebted to Richard Sasiela, who has spent many years developing expressions for the principal anisoplanatic effects. I would also like to thank Robert Kramer, who contributed to the development of the servo-system model, and Jan Herrmann for his frequent involvement in discussions of turbulence theory. Finally, I wish to express my gratitude to Jack Lifsitz, Charles Primmerman, and Darryl Greenwood for their technical and editorial input to this article.

REFERENCES

1. S.M. Farber, "Large Optical Telescopes—New Views into Space and Time," *Ann. N.Y. Acad. Sci.* **422**, 171 (1982).
2. K. Krisciunas, *Astronomical Centers of the World* (Cambridge University Press, Cambridge, MA, 1988).
3. R.W. Smith, *The Space Telescope* (Cambridge University Press, Cambridge, MA, 1989).
4. J.O. Burns, N. Duric, G.J. Taylor, and S.W. Johnson, "Observatories on the Moon," *Sci. Am.* **262**, 42 (Jan. 1990).
5. J.N. Bahcall et al., *The Decade of Discovery in Astronomy and Astrophysics* (National Academy Press, Washington, 1991).
6. A. Kolmogorov, in *Turbulence, Classic Papers on Statistical Theory*, S. K. Friedlander and L. Topper, eds. (Interscience Publishers, New York, 1961).
7. V.I. Tatarski, *Wave Propagation in a Turbulent Medium* (McGraw-Hill, New York, 1961).
8. D.L. Fried, "Limiting Resolution Looking Down through the Atmosphere," *J. Opt. Soc. Am.* **56**, 1380 (1966).
9. H.W. Babcock, "The Possibility of Compensating Astronomical Seeing," *Publ. Astron. Soc. Pac.* **65**, 229 (1953).
10. J.W. Hardy, "Active Optics: A New Technology for the Control of Light," *Proc. IEEE* **66**, 651 (1978).
11. D.P. Greenwood and C.A. Primmerman, "Adaptive Optics Research at Lincoln Laboratory," in this issue.
12. J. Feinleib, Proposal No. 82-P4, Adaptive Optics Associates, Cambridge, MA (1982).
13. R. Foy and A. Labeyrie, "Feasibility of Adaptive Telescope with Laser Probe," *Astron. Astrophys.* **152**, L29 (1985).
14. D.V. Murphy, C.A. Primmerman, B.G. Zollars, and H.T. Barclay, "Experimental Demonstration of Atmospheric Compensation Using Multiple Synthetic Beacons," *Opt. Lett.* **16**, 1797 (1991).
15. R.A. Humphreys, C.A. Primmerman, L.C. Bradley, and J. Herrmann, "Atmospheric-Turbulence Measurements Using a Synthetic Beacon in the Mesospheric Sodium Layer," *Opt. Lett.* **16**, 1367 (1991).
16. D.V. Murphy, "Atmospheric-Turbulence Compensation Experiments Using Cooperative Beacons," in this issue.
17. B.G. Zollars, "Atmospheric-Turbulence Compensation Experiments Using Synthetic Beacons," in this issue.
18. C.A. Primmerman, D.V. Murphy, D.A. Page, B.G. Zollars, and H.T. Barclay, "Compensation of Atmospheric Optical Distortion Using a Synthetic Beacon," *Nature* **353**, 141 (1991).
19. R.Q. Fugate, D.L. Fried, G.A. Ameer, B.R. Boeke, S.L. Browne, P.H. Roberts, R.E. Ruane, G.A. Tyler, and L.M. Wopat, "Measurement of Atmospheric Wavefront Distortion Using Scattered Light from a Laser Guide-Star," *Nature* **353**, 144 (1991).
20. D.P. Greenwood, "Bandwidth Specification for Adaptive Optics Systems," *J. Opt. Soc. Am.* **67**, 390 (1977).
21. R.E. Hufnagel, "Variations of Atmospheric Turbulence," *Dig. of Technical Papers, Topical Mtg. on Optical Propagation through Turbulence, Optical Society of America, Washington, 1974.*
22. J.L. Bufton, "Comparison of Vertical Profile Turbulence Structure with Stellar Observations," *Appl. Opt.* **12**, 1785 (1973).
23. R.J. Noll, "Zernike Polynomials and Atmospheric Turbulence," *J. Opt. Soc. Am.* **66**, 207 (1976).
24. D.P. Greenwood and D.L. Fried, "Power Spectra Requirements for Wave-Front-Compensative Systems," *J. Opt. Soc. Am.* **66**, 193 (1976).
25. F. Roddier, "Curvature Sensing and Compensation: A New Concept in Adaptive Optics," *Appl. Opt.* **27**, 1223 (1988).
26. R.R. Parenti and R.J. Sasiela, "Laser Guide-Star Systems for Astronomical Applications," submitted to *Proc. IEEE.*
27. R.J. Sasiela, "Wavefront Correction Using One or More Synthetic Beacons," submitted to *Proc. IEEE.*
28. D.L. Fried, "Anisoplanatism in Adaptive Optics," *J. Opt. Soc. Am.* 72, 52 (1982).
29. W.L. Wolfe and G.J. Zissis, eds., *The Infrared Handbook* (Environmental Research Institute of Michigan, 1985).
30. G.A. Tyler, "Bandwidth Considerations for Tracking through Turbulence," The Optical Sciences Company, Report No. TR-887 (1988).
31. T.H. Jeys, A.A. Brailove, and A. Mooradian, "Sum Frequency Generation of Sodium Resonance Radiation," *Appl. Opt.* **28**, 2588 (1989).
32. T.H. Jeys, "Development of Mesospheric Sodium Laser Beacon for Atmospheric Adaptive Optics," *Lincoln Laboratory J.* 4, 133 (1991).

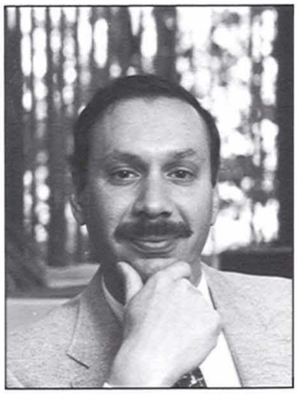

RONALD R. PARENTI
is a staff member in the High-Energy-Laser Beam Control and Propagation group. His area of research is adaptive optics. He received his B.S. degree in physics from Bowling Green State University and his M.S. and Ph.D. degrees in physics from Carnegie Mellon University. Ron has been at Lincoln Laboratory since 1974, and he has been a member of the Innovative Research Program since 1988.